Copper Composites and Laser Sintering: Novel Hybridization Method for 3D Printed Electronics

*Rémi Rafael and Paddy K. L. Chan**

Additive manufacturing of electronic devices is challenging because plastics and metals, which are both required as insulator and conductor, respectively, have very distinct thermal properties. Despite significant research efforts, the currently available electronic-printing methods are still limited by low printing speeds and high manufacturing costs. In this work, a hybrid printing method is proposed that combines fused deposition modeling (FDM) with laser sintering to print thermoplastics and copper in a single process. A copper and copper-oxide composite filament is developed that is compatible with FDM printing. The composite undergoes in situ reduction under laser exposure and produces a highly conductive copper network. Using the home-developed 3D printer, 3D conductive vias embedded in thermoplastic dielectric are demonstrated. The printed copper electrodes have low resistivity of 4×10^{-4} Ω cm and are compatible with soldering. This novel metal-deposition approach and setup prove a novel concept for developing modern electronics using additive manufacturing.

1. Introduction

Additive-manufacturing technologies have been the focus of multidisciplinary research and industrial efforts owing to their attractive potential such as in mass personalization, decentralized manufacturing,[1] reduced environmental effects,[2] and new design strategies.[3] However, to date, the printed parts have remained mostly incapable of electronic functions. In the age of information, when sensors are incorporated in common objects to make them interactive and adaptable for the internet of things, directly integrating electronic components into a three-dimensional (3D) printed object remains challenging.[4]

R. Rafael, P. K. L. Chan
Department of Mechanical Engineering
The University of Hong Kong
Pokfulam Road, Hong Kong China
E-mail: pklc@hku.hk
P. K. L. Chan
Advanced Biomedical Instrumentation Centre
Hong Kong China

The ORCID identification number(s) for the author(s) of this article can be found under https://doi.org/10.1002/admt.202201900

The 3D printing processes for thermoplastics used in mechanical structures, and those for the metals required for electronic interconnections are very different. In particular, most metal-printing methods involve high temperatures (>1000 °C), which are incompatible with common thermoplastics.[5]

Specific conductive materials have been developed to use with existing additive manufacturing techniques. In particular conductive inks composed of metal micro- or nano-particles (generally silver) in suspension in a fluid can be printed by Direct Ink Writing (DIW),[6] inkjet printing,[7] material jetting,[8] or multi-jet fusion.[9] All of these techniques have the capacity to print different materials. By using a dielectric ink as a structural material together with a conductive ink, 3D electronic devices can be manufactured. However, the large-scale use of those techniques for centimeter-scale 3D electronic devices manufacturing is still being limited by the high cost and the sintering step required by conductive inks. As pointed out by Xu et al.[10] the fabrication of solid structures from liquid inks also requires a solidification phase associated with specific challenges. Alternatively, conductive thermoplastic composites have been developed for the fused deposition modeling (FDM) technique[11] but the printed materials have very limited conductivities. The most conductive filament commercially available, Electrifi, exhibits a resistivity of 6×10^{-3} $\Omega \cdot cm$.[11] The Supporting Information Table S1 (Supporting Information) provides more details on all those techniques.

To overcome the aforementioned limitations, Hybrid Additive Manufacturing (HAM) methods have been proposed. HAMs are characterized by the integration of an additive manufacturing technique together with a complimentary fabrication method. The complimentary methods need not be capable of 3D printing, but can be specialized for high-resolution printing or high conductivity materials. In 2012, Lopes et al. first integrated DIW and stereolithography to form 3D structures with embedded electronic circuits made of silver ink.[12] The Voxel 8 printer released in 2015, also integrate DIW with FDM to produce embedded circuitry.[13] More recently smaller nozzles (down to 2 μm) and inks with specific rheology have been developed for high-resolution, free-form DIW on 3D objects.[14] Aerosol jet printing is also a popular choice for integration with FDM or selective laser sintering[15] as it allows non-contact deposition and high resolution (as low as 10 μm).[16,17] Other approaches like the embedding

**ADVANCED
SCIENCE NEWS**

www.advancedsciencenews.com

**ADVANCED
MATERIALS
TECHNOLOGIES**

www.advmattechnol.de

of metal wires,[18–20] laser sintering of dip-coated layers,[21] surface modification with inkjet printing,[22] or the cluster beam deposition of metal particles[23] have been integrated with the FDM technology. Another intense research area for electronic HAM is electroplating as it has the capacity to form high-density and high-conductivity metallic layers on free-form objects. Kim et al.[24] or Lazarus et al.[25] used it to plate the surface of FDM printed conductive composite to lower the resistance of traces and reach conductivities comparable with conventional printed circuit boards. Electroless plating can also be associated with various patterning techniques to produce electrical circuits on 3D surface. For instance, Zhan et al. used FDM to print together a normal and a catalyst loaded ABS material.[26] Once immerged in an electroless plating bath, copper is selectively deposited on the catalyst-loaded area. Alternatively, Esfahani et al.,[27] Balzereit et al.,[28] and Wang et al.[29] used FDM, selective laser sintering, and vat polymerization respectively to print 3D objects out of a single material before using a laser to selectively define the palatable areas.

Given the variety of printing techniques developed, it is necessary to consider the characteristics required for a technology to have practical applications in the industry. Printing resolution and conductivity are critical and often the main focus of research, but design freedom, i.e. the set of rules that the technology imposes on the geometry of the printed parts, is also important. For 3D electronic manufacturing, it is essential to print conductive vias embedded inside the bulk of the printed part. Otherwise, any printed electrical circuit is topologically analogous to a single-layer printed circuit board, and electronic components must be assembled on the surface of the part where they are exposed to damage. To produce embedded electronic, a technique must be able to alternate between printing dielectric and conductive materials. However, this alternance is not always possible. For instance, when integrating powder bed fusion and electroless plating, the printed part must be removed from the powder bed and immersed in an electrolyte. It is then impossible to reinsert the object into the powder and resume the printing process. In other cases, alternance is possible but requires a transfer process that significantly increases printing time, like in the case of cluster beam deposition,[23] where the part must be taken in and out of a vacuum chamber.

In light of these considerations, an interesting research aim consists not in associating different technologies in a sequential order, but rather in their integration into a single process to freely switch between conductive and dielectric materials. In this spirit, Hou et al.[30] developed a copper/high-density-polyethylene (HDPE) powder mixture and changed the printing steps of the selective laser melting process to produce a functional embedded 3D electric circuit. Alternatively, Xiao et al.[31] added a laser diode to a digital light processing (DLP) setup and used it to print a poly-ethylene glycol diacrylate photosensitive resin with a silver nitrate additive. While the UV light source of the DLP projector could polymerize the resin and form a 3D object, the laser diode selectively caused the reduction of the silver nitrate into native silver and formed conductive vias. Despite the low out-of-plane conductivity, this technique successfully demonstrated embedded and 3D circuits.

In this article, we propose a novel approach for printing electronics based on the hybridization of FDM and laser sintering. We developed a homemade FDM printer setup with a laser-sintering function and a copper-based thermoplastic filament that is fully compatible with the traditional FDM technology. This filament, which is composed of native copper(Cu), cuprite oxide (Cu_2O) and copper oxide (CuO) particles, starch, and poly(lactic acid) (PLA), is initially dielectric but becomes highly conductive when exposed to an intense laser radiation, i.e., "sintering." During sintering, PLA and starch disintegrate, and the copper oxides are reduced into native copper, forming a highly conductive interconnected network. By alternating the printing and sintering steps, a complete 3D object that includes both insulative and conductive structures can be layer-by-layer printed. We designed and built a custom 3D printer with two FDM extrusion heads and one laser head. The two extrusion heads print PLA and copper composite, whereas the laser head selectively sinters the printed composite. In this printing setup, we demonstrate a copper network with a resistivity of 4×10^{-4} Ω cm and its capability to print centimeter-scale polymer-conductive 3D objects. As a proof of concept, we implemented our new setup and composite filaments to build a 1-cm-tall 3D conductive circuit and a light-emitting diode (LED) blinking circuit with a silicon-based timer chip and tin soldering.

2. Concept of the Copper Composite

Composite filaments that are composed of thermoplastics and conductive (carbon or metal-based) particles have been studied for many years[32–34] and are considered as among the most economical methods for printing conductive materials.[11,35] In these filaments, the conductive-particle loading is superior to the percolation threshold. As a result, particles that are randomly dispersed in the polymer matrix are interconnected and form conductive paths (a network of contacting particles) in the composite. The conductivity of the composite increases with the conductive-particle loading and aspect ratio of the particles.[36] However, to retain its thermoplastic properties, the composite must simultaneously contain a large amount (>50 vol.%) of polymer matrix,[37–39] which inevitably limits the conductivity of the printed samples. In particular, as presented by Chunyu et al. in the context of carbon-nanotube composites, the presence of a polymer matrix at the intersection between adjacent particles can create tunnel junctions with a resistance that is significantly higher than the direct ohmic contacts.[40] The fundamental concept developed in this work consists of removing the polymer matrix after the printing step, leaving only particles to form a highly conductive network. Because our composite is based on copper, we also investigated the effect of surface oxidation and the potential of the laser for in situ reduction and sintering.

Thermal sintering was previously exploited to create fully dense metal and ceramic objects.[41,42] However, this technology (referred to as "metal fused filament fabrication") requires a high-temperature sintering step of ≈1100 °C[43] in a furnace. Because this temperature is applied to the entire printed part, it is incompatible with plastic–conductive hybrid parts. In the present work, we used laser, instead of mass heating in a furnace, to selectively remove the polymer matrix in a restricted area.

To prove this concept, we employed two commercially available copper-composite filaments, namely, "Copper Filamet" from The Virtual Foundry and "MetalFil-Classic Copper" from Form-Futura. Both filaments are PLA-based composites with 90% and

**ADVANCED
SCIENCE NEWS**

www.advancedsciencenews.com

**ADVANCED
MATERIALS
TECHNOLOGIES**

www.advmattechnol.de

80% (wt.%) copper loading, respectively. After printing 20 × 60 mm^2 flat samples on PLA bases, we alternatively used a 10-W 10.6-µm CO$_2$ laser or a 5.5-W 450-nm blue laser with various combinations of parameters to "sinter" the surface of the samples. The results, which are presented in Figure S1 (Supporting Information), demonstrated that PLA could be successfully removed, leaving a high concentration of copper particles. However, the copper particles became oxidized during the process, and none of the samples yielded a conductive result. Furthermore, the resulting Cu–CuO particles were loosely bonded and could be separated from the sample by scratching or strong airflow.

This result was expected because PLA vaporizes below 450 °C when copper sinters at ≈1100 °C. The energy levels of the two lasers in our experiments were sufficiently high to vaporize PLA but insufficient for thermal sintering (i.e., partially melting) of the copper. Previously numerous investigations that focused on selective laser sintering have demonstrated that an oxygen-deficient atmosphere is required during metal sintering to prevent oxidation.[44,45] The most energy-intensive parameters we tested using the CO$_2$ laser caused the sample to ignite, but the copper particles remained unsintered. These results indicated that traditional sintering by heating the sample close to its melting point is not applicable in the context of polymer–metal mixed printing.

Instead of partial melting, sintering (i.e., bridging adjacent particles) can be achieved by chemical reaction that causes deposition of a native copper layer on copper particles. This effect has been exploited in the context of intense pulsed light (IPL) sintering using copper formate, which is a metal–organic compound.[46,47] Copper formate spontaneously decomposes at approximately 200 °C to form native copper and volatile compounds. Formic acid[48] and ethylene glycol[49] can also induce a reducing effect on CuO under intense light to produce native copper. However, copper formate, formic acid, and ethylene glycol are all incompatible with the temperatures associated with FDM printing (200–250 °C depending on the materials) because a reduction reaction would occur during printing, before the removal of the polymer matrix. Instead, starch and cellulose have been shown to produce various reducing agents during thermal decomposition[50,51] and do not degrade under normal printing temperatures.

To investigate the reducing effect of starch, we mixed CuO and starch powders, spread the mixture on a glass slide, and exposed it to a laser beam. The results, presented in Figure S2 (Supporting Information), revealed that the CuO was reduced, and a conductive copper layer was left. In comparison, copper powder that was exposed under the same conditions without starch became oxidized during the laser treatment (see Figures S3, Supporting Information).

On the basis of these results, we developed a recipe for a composite filament using 55% vol of a PLA matrix and 45 vol.% of mixed particles. The particle mix was composed of 60% (weight ratio) of copper powder, 30% of CuO, and 10% of starch. Supporting Information and Figure S5 (Supporting Information) illustrate the proposed sintering mechanism. PLA was selected as the matrix because it has excellent printing characteristics and very low ash content (almost no residue is left after sintering[52]). Additionally, PLA is cheap and can be bio-sourced and biodegrad-

able. The CuO that we used was in powder form with a mean particle size of 5 µm (see Figure S6, Supporting Information). The copper powder was specifically produced in our laboratory using an electrolytic process to achieve a dendritic structure with a high aspect ratio and small particle size (<20 µm). The starch was alimentation-grade cornstarch.

3. Copper-Powder Preparation

During the tests on the commercially available copper filaments, vaporization of PLA during the laser sintering generated a large amount of gas, which could scatter the particles and inhibit the formation of a conductive network. To solve this problem, we employed electrolytic copper particles with a specific dendrite structure, as shown in **Figure 1**a. This shape ensured that the neighboring particles interlocked together and formed a porous network that allowed the gas to pass through.

The copper-powder-generation setup is shown in Figure 1b with two copper electrodes dipped in a copper sulfate solution.[53] The literature on thermoplastic composite indicates that at equal particle loading, smaller particles improved the flowability of molten composite.[54,55] Additionally, in the context of 3D printing, the particles should be at least one order of magnitude smaller than the dimension of the extrusion nozzle to prevent clogging.[56,57] Therefore, we optimized the electrolysis parameters to minimize the copper-particle size (see Supporting Information for details) and used a 20-µm sieve to remove the large particles.

After synthesis and during the drying process, the copper particles that were in contact with atmospheric oxygen oxidized. Figure 1c shows, on a true color image taken by optical microscopy, multiple red crystals that are typical of cuprite oxide (Cu$_2$O). To confirm the actual composition of the copper powder, we performed an X-ray diffraction (XRD) study, and the results are shown in Figure 1d. We extracted the crystalline-phase composition of 55% Cu, 43% Cu$_2$O, and 2% CuO (weight ratio) using the Profex 5.0.1 software.[58] In the present paper, the expression "copper powder" always refers to this mixture of native copper and oxides, which were obtained after sieving with a 20-µm sieve.

4. Filament Preparation and Printing Setup

To prepare the composite filament for printing, all components [PLA, starch, CuO, and copper powder] were dried and extruded using a twin-screw extruder to create a 1.75 ± 0.1-mm-diameter filament. PLA composite with high-solid-particle loading suffers from increased brittleness, which can cause issues during printing.[59] This brittleness can be quantified based on the minimum radius of curvature before rupture. Our filament with 55% PLA and 45% solid particle volume ratios broke at ≈60 mm compared with the 70 mm (The Virtual Foundry) and 10 mm (Form-Futura) of the two commercial copper composites (see Figure S7, Supporting Information). To address this fragility, we developed a special 25-cm diameter spool to roll our composite filament and designed a low-friction spool holder to minimize the tensions. We never experienced filament breaking during the printing process using this mechanism.
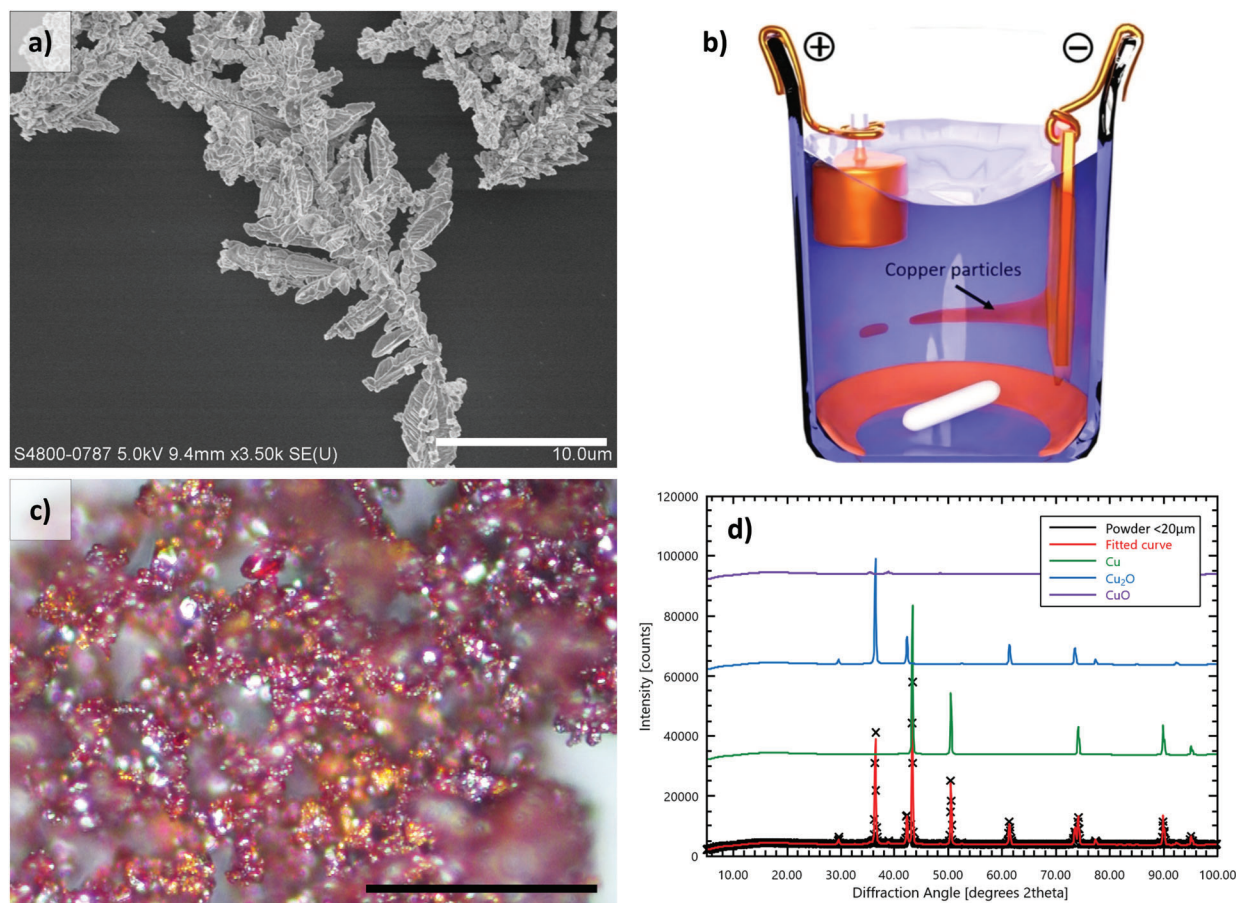
**ADVANCED
SCIENCE NEWS**

www.advancedsciencenews.com

**ADVANCED
MATERIALS
TECHNOLOGIES**

www.advmattechnol.de

Figure 1. a) Scanning Electron Microscope image of a dendrite-shaped copper particle synthesized by electrolysis. b) Schematic illustration of our electrolytic copper-particle-generation setup. c) Picture of our sieved copper powder taken by optical microscopy. Scale bar: 100 μm. d) XRD scan of the copper powder. The raw data points in black are superimposed with the fit achieved using the PROFEX software. The green, blue, and purple curves correspond to the components of this fit associated with Copper, Cuprite oxide, and copper oxide, respectively

Figure 2a shows the schematic drawing of our custom 3D printer and photographs of the major components. Developed at below USD 1000.00, this design used commercially available printer parts. The concept and composition details of the printer are provided in Figure S8 (Supporting Information). Figure 2b illustrates how the three printer tools are used to print dielectric and composite filaments, as well as selectively sinter the composite. The G-codes (printing files) were generated using open-source slicer software Ultimaker Cura 4.9.1 and modified using custom Python routines. The strategy used to create the G-codes to be compatible with the FDM–laser hybrid printing is further described in Supporting Information. To minimize the clogging issue, the composite filament was printed through a 0.6-mm nozzle (the line width was accordingly set to 0.6 mm). The layer height was set to 0.1 mm to match the sintering depth (discussed later in this paper). The other printing parameters are provided in Experimental Section.

5. Sintering Parameters

The most critical step of our hybrid printing method was the laser sintering, in which the initially dielectric composite turned into

a conductive composite. Our laser for those experiments was a 450 nm continuous wave, blue laser diode with a 5.5W nominal maximum optical power. The other parameters associated with this sintering were the laser spot size (i.e., focus), hatch distance (distance between two successive laser scans), scanning speed, laser power, and number of sintering passes.

The focus and hatch distance were interdependent because the hatch must be smaller than the laser spot size to achieve homogeneous sintering. In these experiments, the hatch distance was set to 150 μm, and the focus lens of the laser module was tuned to achieve a homogeneously sintered layer after three scans. The laser spot was then ≈260 μm (see Figure S9, Supporting Information). The focus and hatch were kept constant in all experiments.

To investigate the effects of the other parameters, we printed a 20×60 mm^2 flat sample composed of a 0.6-mm composite layer on top of a 0.8-mm pure PLA base, as shown in **Figure 3**a (the two FDM heads allowed the use of two distinct materials). A PLA base was used to ensure mechanical robustness of the sample, reduce the composite thickness, and save the filament. A white PLA filament was selected because it is not degraded by exposure to blue laser even under the most energy-intensive parameters (see Figure S10, Supporting Information). To minimize the effects of
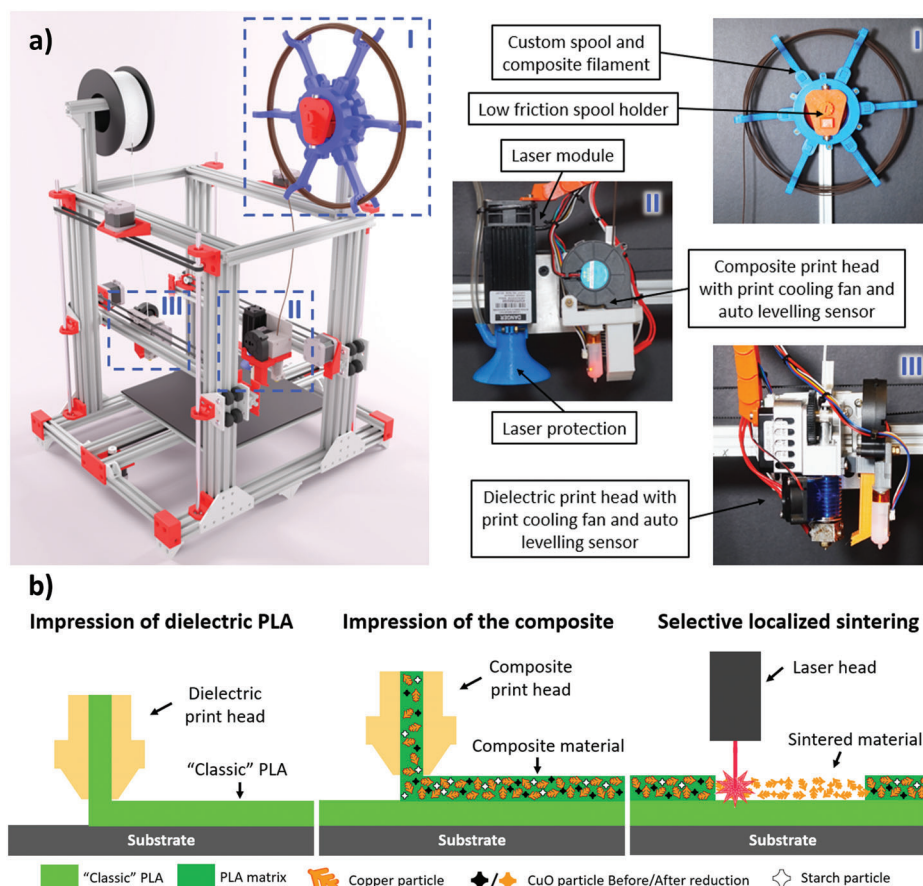
**ADVANCED
SCIENCE NEWS**

www.advancedsciencenews.com

**ADVANCED
MATERIALS
TECHNOLOGIES**

www.advmattechnol.de

Figure 2. a) Computer-generated image of our hybrid printer and photographs of the main components. b) schematic illustration of the three functions of the hybrid printer i) impression of the dielectric PLA, ii) impression of the composite, and iii) selective localized sintering.

surface rugosity, the samples were printed using the "ironing" option of the Cura slicer (details can be found in Figure S11, Supporting Information). After the samples were printed, we used the laser to sinter the shape of 1×10 mm^2 electrodes that were terminated with 1.5×1.5 mm^2 square pads on either side.

Multiple electrodes were sintered while the laser power was varied from 10% to 100% at a 10% increment (the maximum nominal output was 5.5 W). The scan speed was varied from 5 to 40 mm s^{-1} at a 5 mm s^{-1} increment step, and the total number of sintering was varied from one to five. The resistance of the individual electrodes measured, using a digital multimeter, is shown in Figure 3b. The data are presented as stacked 3D maps in which the laser power and laser speed represent the X and Y axes, respectively, and the resistance represents the Z and color axes. The five maps obtained using one to five sintering steps were stacked with offset in the Z direction to facilitate reading. We observed that for a given number of sintering, the lowest resistance was always achieved with the most energy-intensive parameters (5 mm s^{-1} and 100% laser power). The variability of the resistance measurements is discussed in Supporting Information and Figure S12 (Supporting Information).

Figure 3c shows the resistance as a function of the total energy received by the sample (summation of the energy at each sintering step). The overall lowest resistance was achieved in five sintering steps at a resistance of 0.4 Ω.

Because increasing the sintering number demonstrated continuous decreasing trend in the resistance, we further investigated the effect of the number of sintering steps while maintaining the speed at 5 mm s^{-1} and laser power at 100%. Figure 3d shows the average resistance of ten samples as a function of the number of sintering steps and an optical image of the electrodes sintered under these conditions. We could observe that the resistance continued to decrease and reached a minimum of 0.27 Ω after six sintering steps. Simultaneously, a reddish-brown layer began to grow on the surface of the electrode after four sintering steps.

To confirm the nature of this layer, XRD scans were performed for each set of sintering conditions (Figure S13, Supporting Information). The composition extracted by fitting from these scans is shown in Figure 3e. Up to four sintering steps, the percentage of copper oxides (Cu$_2$O and CuO) continuously decreased, and the proportion of the native copper reached a maximum value at four sintering steps. Thereafter, the proportion of cuprite oxide gradually increased.

This result confirmed that the decomposition of PLA and starch during the laser sintering reduced oxides. After four sintering steps, mainly the copper and copper oxides remained at the surface of the sintered area. Upon further exposure to the laser, this top surface again oxidized due to atmospheric oxygen. For this reason, we considered the optimal sintering conditions
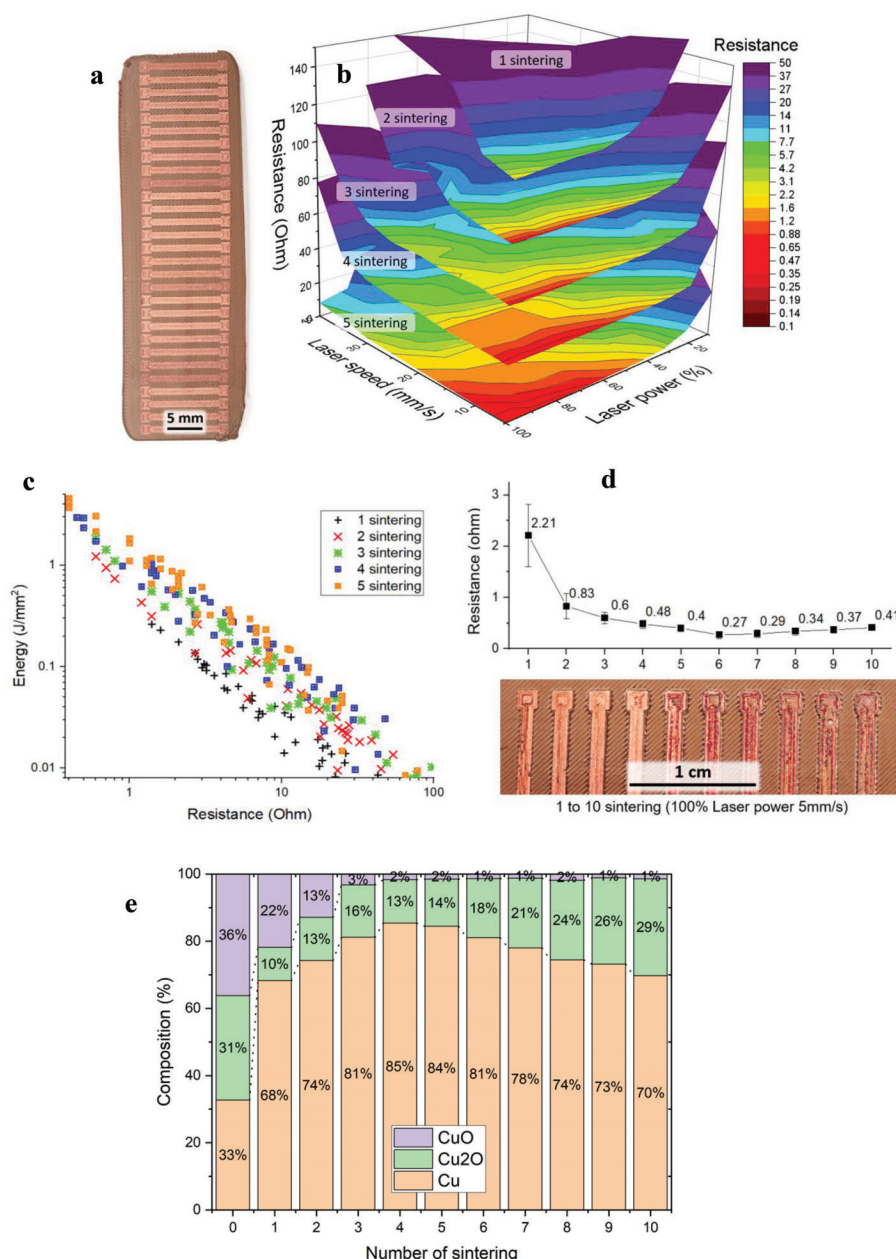
ADVANCED
SCIENCE NEWS

www.advancedsciencenews.com

ADVANCED
MATERIALS
TECHNOLOGIES

www.advmattechnol.de

Figure 3. a) Picture of a composite sample with electrodes sintered on the surface. b) Stacked three-dimensional maps of the resistance of a 1×10 mm^2 electrode as a function of sintering parameters. c) Representation of the resistance of an electrode as a function of the total energy per surface unit. d) Resistance of an electrode sintered at 100% laser power at 5 mm s^{-1} as a function of the number of sintering steps and pictures of the corresponding electrodes. The resistance value is an average value over 10 samples. The error bar is one standard variation. e) Composition of the sintered composite as a function of the number of sintering steps (100% laser power at 5 mm s^{-1}) extracted by fitting X-ray diffraction scans. The original scans are presented in Figure S13, Supporting Information.

to be 5 mm s^{-1}, 100% laser power, and 4 sintering, where the resistance achieved is the lowest before the "re-oxidation" of the sintered copper. The oxidation after multiple sintering implied that increasing the laser power and keeping the number of sintering steps small were preferable to achieve low resistance. More detailed investigations on higher laser power and composition of the filaments to further optimize the printer-sample resistance are ongoing and will be reported later.

6. Properties of Sintered Layer and 3D Interconnections

Because PLA accounted for 55% vol of the composite, its removal left a porous copper structure. **Figure 4**a represents a scanning electron microscopy image of the composite top surface after four sintering steps at 100% laser power and laser-scanning speed of 5 mm s^{-1}. This figure shows regularly dispersed
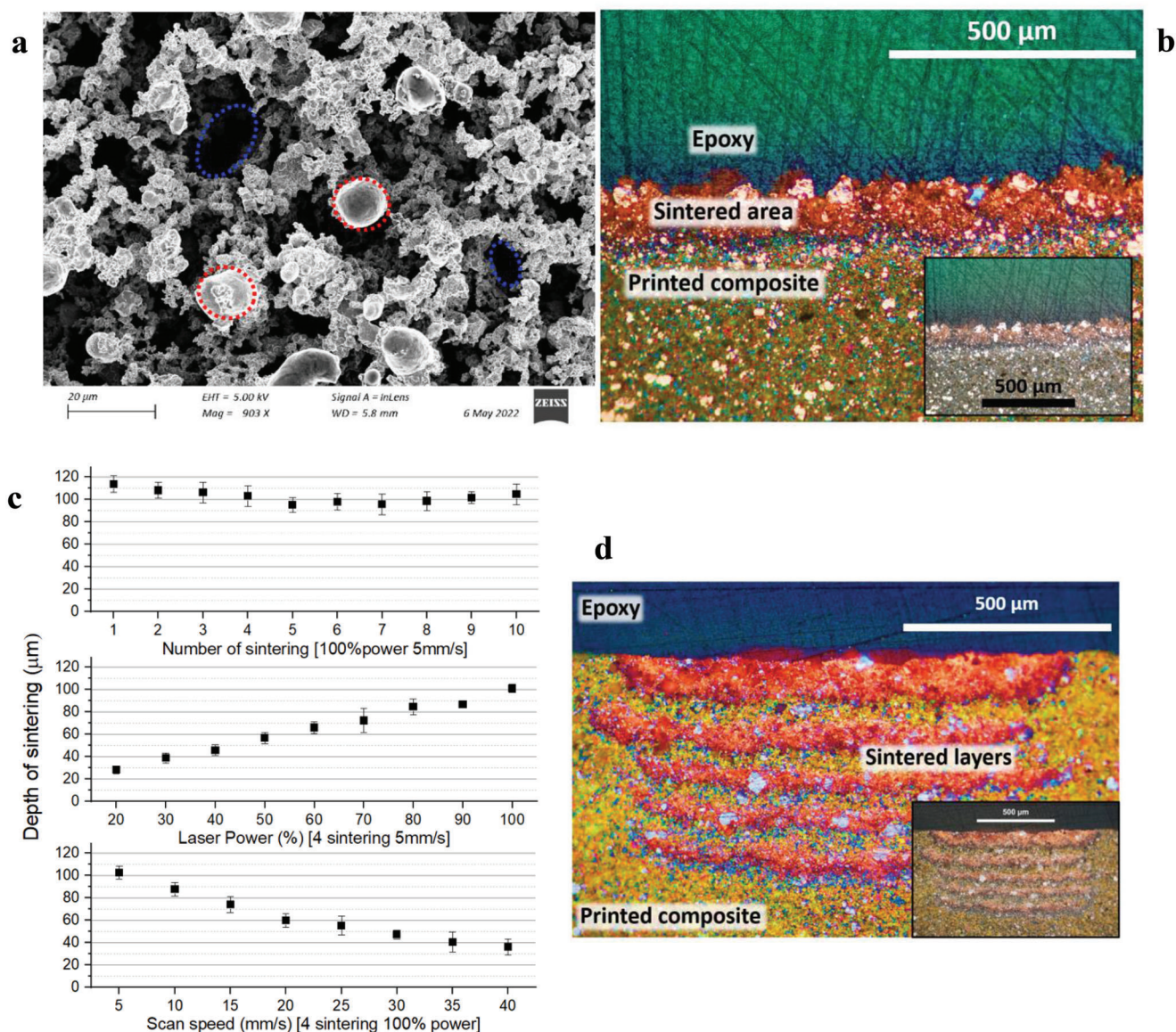
**ADVANCED
SCIENCE NEWS**

www.advancedsciencenews.com

**ADVANCED
MATERIALS
TECHNOLOGIES**

www.advmattechnol.de

Figure 4. a) Scanning Electron Microscope image of the top surface of the composite sintered four times at 100% laser power and 5 mm s^{-1}. For visualization, two pores are circled in blue and two spherical copper particles are circled in red. b) Cross section of the sintered composite in enhanced color (real color in the inset) obtained by optical microscopy. c) Depth of sintering of the different laser parameters measured at the cross sections. Each point is an average of six measurements. The error bar is one standard deviation. In each graph, one parameter is varied. The other parameter value is indicated between brackets. d) Cross section of the five superposed sintered composite layers in enhanced color (real color in the inset)

pores with a typical dimension of ≈10 µm. These pores were formed during the expulsion of the volatile PLA disintegration products generated during sintering. At the top surface of the copper network, some round particles were also visible. These copper-based particles were not part of the initial composite and were formed during sintering. Their spherical geometries suggested that they were the result of local melting. Examples of these particles and pores are circled in red and blue in the figure.

The sintering depth also played an important role in evaluating the conductance of the printer copper network. To measure it, we embedded the samples into epoxy resin and cut it perpendicular to the electrodes to expose the cross-section. After the cut sur-

face was polished, optical microscopy was employed to observe the sintered area. Figure 4b shows the cross-section of an electrode in enhanced colors. The sintered region is clearly visible in a reddish color. Employing the ImageJ software, we extracted the thickness of this layer under various sintering conditions (Figure 4c). The depth of the sintered layer increased with the laser power and decreased with the scan speed. However, it did not strongly depend on the number of sintering steps. This result implied that the laser energy was absorbed and/or reflected by the upper surface and not transmitted into the composite (at least in the 450-nm wavelength). Accordingly, the region affected by the laser depended on the thermal (not optical) propagation of the energy.
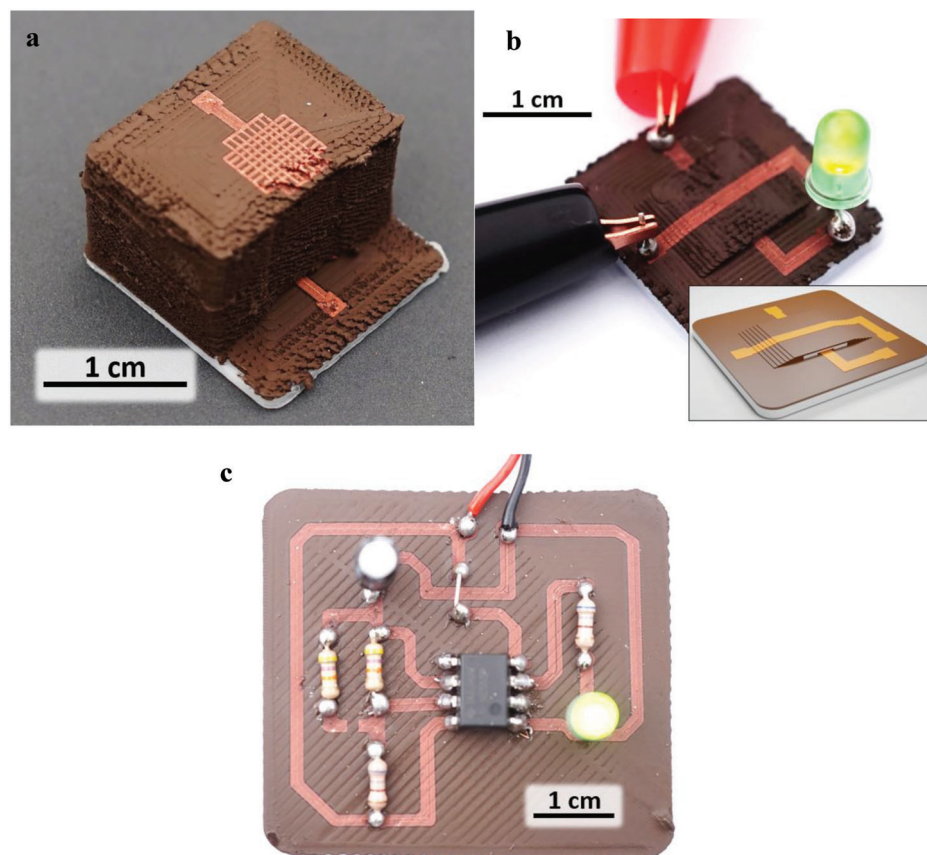
Figure 5. a) Picture of a printed sample using a "grid pattern-based" Z via. The resistance between the top and bottom electrodes separated by 1 cm (i.e., 100 printed layers) is 33 Ω. b) Picture of a sample using a slope to allow conductive traces to cross each other. Inset: Schematic drawing of the printed sample. c) Picture of a simple electronic circuit using soldered conventional components to flash a LED (video provided as Supporting Information)

The average resistance of the composite sintered under optimal conditions was 0.4 Ω for a 10-mm-long and 1-mm-wide electrode. With a sintering depth of 100 μm, the typical resistivity of this material was 4×10^{-4} Ω cm, two orders of magnitude higher than the resistivity of bulk copper (1.71×10^{-6} Ω cm international annealed copper standard). This value is explained by the porous nature of the copper network. These electrodes did not deteriorate under a current of 0.6 A that was maintained for 1 h (see Figure S14, Supporting Information), which was sufficient for electronic and circuit applications.

To apply this technique to 3D printing, we stacked sintered layers on top of each other to generate a 3D conductive pathway. When the printed-layer thickness was equal to or less than the sintering depth, the entire printed composite could be sintered; hence, a good electrical contact in the Z direction was achieved. Figure 4d shows the cross-section of the five stacked layers printed at a 0.1-mm-layer height and sintered on top of each other. To create this sample, each layer was successively printed and sintered before the following layer was printed. The resistance between the first and fifth layers was less than 1.8 Ω (see Figure S15, Supporting Information).

However, we could notice that the sintered lower layers were compressed when the upper layers were printed at the top. This phenomenon was particularly visible when the thicknesses of the top and third layers were compared, as shown in Figure 4d:

Printed and sintered under the same conditions, these layers showed the same initial thickness, but the porous copper structure was compressed by the pressure of the molten composite during the subsequent printing steps. This phenomenon (which was dependent on the printing parameters) affected the conductivity of the lower layers by breaking a portion of the copper network junctions and thickness of the upper layers. Instead, of being compressed between the nozzle and underlayer, the molten composite occupied the space that was freed by crushing the underlayer. The resulting layer was thicker, and pores can appear. During printing on large, sintered areas, these defects accumulate and cause printing failure (see Figure S16, Supporting Information). The molten-composite pressure could be reduced by increasing the layer thickness. However, this solution requires the capability to sinter this entire layer.

Compression of the sintered layer due to the pressure of the extruded composite could be prevented using a grid pattern (see Figure S17, Supporting Information). This pattern, which is shown in **Figure 5**a, ensured that a portion of the composite remained unsintered and mechanically strong to support the conductive copper mesh. By using this structure, we could print conductive vias oriented in the Z direction. The example shown in Figure 5a had a total thickness of 1 cm and a resistance of 33 Ω between the upper and lower sintered planes.

At smaller step heights, the sintering process produced continuous paths over steps of 0.1 mm. By relying on this property, we could connect different layers using slopes. Figure 5b shows this process. A bridge with a 15° slope was used to allow crossing of two distinct traces. The second trace (which passed on top of the bridge) was sintered after the whole part has been printed (details available in Figure S18, Supporting Information)).

The sintered composite was compatible with the soldering process. Figure 5c shows a photograph of a simple circuit that integrated conventional resistances, a capacitor, and a 555-timer microchip to make a LED flash. All components were assembled using a soldering iron and tin solder. Video S1 and Figure S19 (Supporting Information) demonstrate how laser sintering could be used to reconfigure this printed circuit and change the blinking frequency.

7. Conclusion

In this work, we developed a novel strategy for 3D printing of conductive and dielectric materials together based on FDM additive manufacturing and laser sintering. We developed a new composite filament that relied on in situ reduction of copper oxides to produce highly conductive copper networks. By employing a custom printer, we could sinter the composite at each layer of the printing process and produce 3D conductive vias that were integrated inside a dielectric printed object. Owing to its low resistivity (4×10^{-4} Ω cm) and high maximum current density (6 A mm^{-2}), the sintered material could be an excellent candidate as electrodes and interconnects or for the development of embedded electronic components. We believe that the methodology and tools proposed in the current study can play an important role in the development of novel fabrication methods for next-generation 3D electronics.

8. Experimental Section

Copper-Powder-Generation Process: The electrolyte was prepared by dissolving 15 g of copper-chloride pentahydrate in 600 mL of deionized water. A rectangular copper electrode was used at the reduction side. The dimensions of the immersed part were $10 \times 40 \times 1.5$ mm^3. On the other side, the electrode consisted of two roughly cylindrical copper ingots whose respective diameter and height were both 22 mm. The ingots were maintained in the electrolyte using copper wires so that only the top surface of the ingot emerged. Both electrodes were separated by 50 mm inside a closed glass container. This container was itself placed in a large box filled with 6 L of water to increase thermal dissipation and control the temperature. The copper ingots were replaced when approximately 80% of their mass was consumed. A DC power supply, i.e., KPS605DF, from Wanptek, was used to apply a constant current flow through the system. A magnetic bar was added to the system, and the stirring speed was adjusted to break the copper dendrites and keep the voltage bias at 15 ± 5 V. When the reaction was initiated at ambient temperature, the system resistance was high, and biases up to 60 V were applied. The system was then heated up in ≈ 25 min, and the temperature stabilized at 45 ± 10 °C. After 5–10 h, the powder that accumulated in the container had to be pipetted out to prevent pseudo-short circuit and local ebullition. A quantitative description of the formed powder is available in Supporting Information.

Extrusion of the Copper Composite: The PLA pellets purchased from Xiamen Keyuan Plastic Co. were ground to less than 500-μm particle size using an IKA MF 10 grinder. This step was performed to promote homogeneous mixing of all component powders and to achieve uniform repar-

tition in the composite while minimizing the hot mixing time (it was observed that prolonged passage in the extruder led to the production of gases and reduction of copper oxides, which were presumably due to the degradation of PLA and/or starch). After drying for one night in a food dehydrator at 68 °C, 100 g of PLA powder was mixed with 217 g of copper powder, 108-g CuO, and 36-g starch. The used CuO was 99% copper(II) oxide from J&K Scientific. The starch used was general-alimentation-grade Meadow cornstarch. The powders were thoroughly mixed before being extruded in a PRISM TSE 16 TC twin-screw extruder. From the feeding side to the extrusion side, the programmed temperatures in the controllers in each of the five zones were 165, 180, 185, 190, and 175 °C. The filament product was cooled using air and water, and driven by a belt puller. The belt speed was manually adjusted to obtain a 1.75-mm-diameter filament.

Detailed Printing Parameters: In all printing processes, the bed temperature was set to 50 °C, and a prime tower was included with a minimum extrusion volume of 6 mm^3. No build plate-adhesion feature, supports, or ooze shield was used.

Dielectric PLA (white PLA from LANBO) was printed using a 0.4-mm nozzle (the line width was set to 0.4 mm) at 204 °C with 100% infill. The layer height was 0.2 mm, and the printing speed was 60 mm s^{-1}, which was reduced to 30 mm/s for the outer layers. A print cooling fan was used after the first layer. The standby temperature was set to 175 °C.

The composite filament was printed using a 0.6-mm nozzle (the line width was set to 0.6 mm) at 215 °C. The wall thickness was set to 100 mm (the entire printed part was considered a wall) to ensure that the printing direction was aligned to the main direction of the printed feature and to minimize holes. The layer height was 0.1 mm, and the printing speed in all feature types was 20 mm s^{-1}. The flow rate was set to 105% to remove any holes in the printed layer. The movement speed was reduced to 40 mm s^{-1} to limit the efforts imposed on the brittle filament. A small coating volume of 0.1 mm^3 was employed with a coasting speed of 80%. The retraction distance was set to 1 mm with 1-mm^3 extra prime amount. The cooling fan was disabled for the composite, and the standby temperature was set to 150 °C.

XRD Scan-Fitting Processes: All XRD scans were carried out on a Rigaku SmartLab in Bragg Brentano configuration between 5° and 100° at a scan speed of 8° min^{-1} and sampling rate of 10 points per degree. The copper source was driven at 45 kV and 200 mA with a nickel K–β filter on the path of the secondary beam. Profex 5.0.1 was used to fit the results. The phase profiles used for the Cu and CuO phases were References 04-009-2090 and 04-007-1375, respectively, from the PDF-4+ database. The profile of the Cu_2O phase was retrieved from the Crystallography Open Database where it was referenced under Code 9007497.

Supporting Information

Supporting Information is available from the Wiley Online Library or from the author.

Acknowledgements

Conflict of Interest

The technology described in this article is currently under evaluation for a patent.

Data Availability Statement

The data that support the findings of this study are available from the corresponding author upon reasonable request.;

**ADVANCED
SCIENCE NEWS**

www.advancedsciencenews.com

**ADVANCED
MATERIALS
TECHNOLOGIES**

www.advmattechnol.de

Keywords

[1] T. Rayna, L. Striukova, *Technol Forecast Soc Change* **2021**, *164*, 120483.

[2] J. P. Rett, Y. L. Traore, E. A. Ho, *Adv. Eng. Mater.* **2021**, *23*, 2001472.

[3] B. Shaqour, M. Abuabiah, S. Abdel-Fattah, A. Juaidi, R. Abdallah, W. Abuzaina, M. Qarout, B. Verleije, P. Cos, *Int J Adv Manuf Technol* **2021**, *114*, 1279.

[4] F. P. Chietera, R. Colella, L. Catarinucci, *Electron.* **2022**, *64*, https://doi.org/10.3390/electronics11010064.

[5] V. Chahal, R. M. Taylor, *Virtual Phys. Prototyp.* **2020**, *15*, 227.

[6] M. Abas, Q. Salman, A. M. Khan, K. Rahman, *J. Brazilian Soc. Mech. Sci. Eng.* **2019**, *41*, 563.

[7] J. Zhang, M. Ahmadi, G. Fargas, N. Perinka, J. Reguera, S. Lanceros-Méndez, L. Llanes, E. Jiménez-Piqué, **2022**, *234*, https://doi.org/10.3390/met12020234.

[8] D. S. Vorunichev, in *2021 Int. Conf. Qual. Manag. Transp. Inf. Secur. Inf. Technol.*, IEEE, **2021**, pp. 476–479.

[9] J. A. Wittkopf, K. Erickson, P. Olumbummo, A. Hartman, H. Tom, L. Zhao, *Int. Conf. Digit. Print. Technol.* **2019**, *2019-Septe*, 29.

[10] X. Xu, J. Yang, W. Jonhson, Y. Wang, A. Suwardi, J. Ding, C. Guan, D. Zhang, *Addit. Manuf.* **2022**, *56*, 102939.

[11] P. F. Flowers, C. Reyes, S. Ye, M. J. Kim, B. J. Wiley, *Addit. Manuf.* **2017**, *18*, 156.

[12] A. Joe Lopes, E. MacDonald, R. B. Wicker, *Rapid Prototyp. J.* **2012**, *18*, 129.

[13] S. Zhen, R. M. Bilal, A. Shamim, *2017 Int. Symp. Antennas Propagation, ISAP 2017*, **2017**, 2017-Janua, 1.

[14] Y. Park, I. Yun, W. G. Chung, W. Park, D. H. Lee, J. Park, *Adv. Sci.* **2022**, *9*, 2104623.

[15] G. L. Goh, V. Dikshit, R. Koneru, Z. K. Peh, W. Lu, G. D. Goh, W. Y. Yeong, *Int J Adv Manuf Technol* **2022**, *120*, 2573.

[16] M. Seiti, O. Degryse, E. Ferraris, *Mater Today Proc* **2022**, *38*, https://doi.org/10.1016/j.matpr.2022.08.488.

[17] D. R. Hines, Y. Gu, A. A. Martin, P. Li, J. Fleischer, A. Clough-Paez, G. Stackhouse, A. Dasgupta, S. Das, *Addit. Manuf.* **2021**, *47*, 102325.

[18] K. M. M. Billah, J. L. Coronel, M. C. Halbig, R. B. Wicker, D. Espalin, *IEEE Access* **2019**, *7*, 18799.

[19] J. L. Coronel, K. H. Fehr, D. D. Kelly, D. Espalin, R. B. Wicker, in *Micro-Nanotechnol. Sensors, Syst. Appl. IX* (Eds.: T. George, A. K. Dutta, M. S. Islam), **2017**, p. 101941F.

[20] C. Kim, C. Sullivan, A. Hillstrom, R. Wicker, *Int. J. Precis. Eng. Manuf.* **2021**, *22*, 919.

[21] E. Olsen, L. Overmeyer, *Flex. Print. Electron.* **2021**, *6*, 015006.

[22] D. J. Roach, C. Roberts, J. Wong, X. Kuang, J. Kovitz, Q. Zhang, T. G. Spence, H. J. Qi, *Addit. Manuf.* **2020**, *36*, 101544.

[23] A. Bellacicca, T. Santaniello, P. Milani, *Addit. Manuf.* **2018**, *24*, 60.

[24] M. J. Kim, M. A. Cruz, S. Ye, A. L. Gray, G. L. Smith, N. Lazarus, C. J. Walker, H. H. Sigmarsson, B. J. Wiley, *Addit. Manuf.* **2019**, *27*, 318.

[25] N. Lazarus, S. S. Bedair, S. H. Hawasli, M. J. Kim, B. J. Wiley, G. L. Smith, *Adv. Mater. Technol.* **2019**, *4*, 1900126.

[26] J. Zhan, T. Tamura, X. Li, Z. Ma, M. Sone, M. Yoshino, S. Umezu, H. Sato, *Addit. Manuf.* **2020**, *36*, 101556.

[27] R. N. Esfahani, M. P. Shuttleworth, V. Doychinov, N. J. Wilkinson, J. Hinton, T. D. A. Jones, A. Ryspayeva, I. D. Robertson, J. Marques-Hueso, M. P. Y. Desmulliez, R. A. Harris, R. W. Kay, *Addit. Manuf.* **2020**, *34*, 101367.

[28] S. Balzereit, F. Proes, V. Altstädt, C. Emmelmann, *Addit. Manuf.* **2018**, *23*, 347.

[29] P. Wang, J. Li, G. Wang, L. He, J. Yang, C. Zhang, Z. Han, Y. Yan, *Addit. Manuf.* **2023**, *63*, 103388.

[30] S. Hou, S. Qi, D. A. Hutt, J. R. Tyrer, M. Mu, Z. Zhou, *J. Mater. Process. Technol.* **2018**, *254*, 310.

[31] J. Xiao, D. Zhang, Q. Guo, J. Yang, *Adv. Mater. Technol.* **2021**, *6*, 1.

[32] Z. Lei, Z. Chen, Y. Zhou, Y. Liu, J. Xu, D. Wang, Y. Shen, W. Feng, Z. Zhang, H. Chen, *Compos. Sci. Technol.* **2019**, *180*, 44.

[33] J. C. Tan, H. Y. Low, *Addit. Manuf.* **2018**, *23*, 294.

[34] B. Podsiadły, P. Matuszewski, A. Skalski, M. Słoma, *Appl. Sci.* **2021**, *11*, 1272.

[35] J. Gong, O. Seow, C. Honnet, J. Forman, S. Mueller, in *34th Annu. ACM Symp. User Interface Softw. Technol.*, ACM, New York, NY, USA, **2021**, pp. 1063–1073.

[36] Y. Chen, F. Pan, S. Wang, B. Liu, J. Zhang, *Compos. Struct.* **2015**, *124*, 292.

[37] J. C. Tan, H. Y. Low, *Addit. Manuf.* **2020**, *36*, 101551.

[38] X. Wang, M. Jiang, Z. Zhou, J. Gou, D. Hui, *Compos. Part B Eng.* **2017**, *110*, 442.

[39] I. Blanco, *J. Compos. Sci.* **2020**, *4*, 42.

[40] C. Li, E. T. Thostenson, T. W. Chou, *Appl. Phys. Lett.* **2007**, 223114, https://doi.org/10.1063/1.2819690.

[41] S. Roshchupkin, A. Kolesov, A. Tarakhovskiy, I. Tishchenko, *Mater Today Proc.* **2021**, *38*, 2063.

[42] C. Tosto, J. Tirillò, F. Sarasini, G. Cicala, *Appl. Sci.* **2021**, *11*, 1444.

[43] M. Mohammadizadeh, H. Lu, I. Fidan, K. Tantawi, A. Gupta, S. Hasanov, Z. Zhang, F. Alifui-Segbaya, A. Rennie, *Inventions* **2020**, *5*, 44.

[44] C. Silbernagel, L. Gargalis, I. Ashcroft, R. Hague, M. Galea, P. Dickens, *Addit. Manuf.* **2019**, 100831, https://doi.org/10.1016/j.addma.2019.100831.

[45] M. Abdelhafiz, K. S. Al-Rubaie, A. Emadi, M. A. Elbestawi, *Materials (Basel).* **2021**, *14*, 2945.

[46] M. Joo, B. Lee, S. Jeong, M. Lee, *Appl. Surf. Sci.* **2011**, *258*, 521.

[47] P. H. Chiu, W. H. Cheng, M. T. Lee, K. Yasuda, J. M. Song, *Nanomaterials* **2021**, *11*, 1864.

[48] W.-H. Cheng, P.-H. Chiu, Y.-J. Li, M.-T. Lee, K. Yasuda, J.-M. Song, **2021**, *2*, 11.

[49] B. Kang, S. Han, J. Kim, S. Ko, M. Yang, *J. Phys. Chem. C* **2011**, *115*, 23664.

[50] G. Qin, A. Watanabe, H. Tsukamoto, T. Yonezawa, *Jpn. J. Appl. Phys.* **2014**, *53*, 096501.

[51] X. Liu, Y. Wang, L. Yu, Z. Tong, L. Chen, H. Liu, X. Li, *Starch – Stärke* **2013**, *65*, 48.

[52] T. Ohkita, S.-H. Lee, *J. Appl. Polym. Sci.* **2006**, *100*, 3009.

[53] R. K. Nekouei, F. Rashchi, A. A. Amadeh, *Powder Technol..* **2013**, *237*, 165.

[54] F. Ippolito, G. Hübner, T. Claypole, P. Gane, *Appl. Sci.* **2021**, *11*, 641.

[55] M. Ahmadifar, K. Benfriha, M. Shirinbayan, A. Tcharkhtchi, *Appl. Compos. Mater.* **2021**, *28*, 1335.

[56] T. Beran, T. Mulholland, F. Henning, N. Rudolph, T. A. Osswald, *Addit. Manuf.* **2018**, *23*, 206.

[57] B. P. Croom, A. Abbott, J. W. Kemp, L. Rueschhoff, L. Smieska, A. Woll, S. Stoupin, H. Koerner, *Addit. Manuf.* **2021**, *37*, 101701.

[58] N. Doebelin, R. Kleeberg, *J. Appl. Crystallogr.* **2015**, *48*, 1573.

[59] S.-Y. Fu, X.-Q. Feng, B. Lauke, Y.-W. Mai, *Compos. Part B Eng.* **2008**, *39*, 933.

2201900 (10 of 10)